Neurobiology of Disease

Symmetry of Cortical Folding Abnormalities in Williams Syndrome Revealed by Surface-Based Analyses

David C. Van Essen,[1] Donna Dierker,[1] A. Z. Snyder,[2] Marcus E. Raichle,[2] Allan L. Reiss,[3] and Julie Korenberg[4]

Departments of [1]Anatomy and Neurobiology and [2]Radiology and Neurology, Washington University School of Medicine, St. Louis, Missouri 63110, [3]Neuroimaging Laboratory, Department of Psychiatry and Behavioral Sciences, Stanford University School of Medicine, Stanford, California 94305, and [4]Cedars-Sinai Medical Center, Los Angeles, California 90048

We analyzed folding abnormalities in the cerebral cortex of subjects with Williams syndrome (WS), a genetically based developmental disorder, using surface-based analyses applied to structural magnetic resonance imaging data. Surfaces generated from each individual hemisphere were registered to a common atlas target (the PALS-B12 atlas). Maps of sulcal depth (distance from the cerebral hull) were combined across individuals to generate maps of average sulcal depth for WS and control subjects, along with depth-difference maps and *t*-statistic maps that accounted for within-group variability. Significant structural abnormalities were identified in 33 locations, arranged as 16 bilaterally symmetric pairs plus a lateral temporal region in the right hemisphere. Discrete WS folding abnormalities extended across a broad swath from dorsoposterior to ventroanterior regions of each hemisphere, in cortical areas associated with multiple sensory modalities as well as regions implicated in cognitive and emotional behavior. Hemispheric asymmetry in the temporal cortex is reduced in WS compared with control subjects. These findings provide insights regarding possible developmental mechanisms that give rise to folding abnormalities and to the spectrum of behavioral characteristics associated with WS.

Key words: **cerebral cortex; morphometry; sulcus; gyrus; cognition; development; language; hemisphere; genetics; spatial cognition**

Introduction

Williams syndrome (WS), a neurodevelopmental condition caused by a hemideletion in chromosome 7 (band 7q11.23), is associated with an unusual pattern of strengths and weaknesses in cognitive abilities. The deficits include impairments in visual–spatial, mathematical, and problem-solving abilities. These are coupled with relative sparing of many other functions and with unusual characteristics such as hyperaffiliative social behavior, atypical expressive language, and enhanced musical interest (Bellugi et al., 2000). The neurobiological basis of this complex set of characteristics has been investigated in a number of recent neuroimaging studies. Morphometric studies have demonstrated a smaller overall brain volume (by 11–13%) in WS compared with control groups plus numerous localized differences in gray matter distribution (particularly in the left hemisphere) and in the size of particular subregions of the cerebral cortex, cerebellar cortex, and subcortical structures (Reiss et al., 2000, 2004; Eckert et al., 2005; Thompson et al., 2005). The reduction in subcortical white matter (18%) markedly exceeds that of gray matter (Thompson et al., 2005), which may be related to increased gyrification (Schmitt et al., 2002). In addition, an increased average cortical thickness has been reported for a broad region of the occipital and temporal cortex almost exclusively in the right hemisphere, along with bilateral differences in "fractal complexity" of cortical folding (Thompson et al., 2005). Functional studies have revealed abnormal functional magnetic resonance imaging (fMRI) activations in restricted regions of the parietal, temporal, and frontal cortices when tested by visuospatial, face-processing, and attentional tasks (Meyer-Lindenberg et al., 2004, 2005b; Mobbs et al., 2004).

Given these morphological and functional differences, it is natural to wonder whether WS is associated with localized changes in the pattern of cortical folding (Bellugi et al., 2000; Galaburda et al., 2001). To address this issue systematically across the entire cortical mantle, analysis methods are needed that can cope with the complexity of convolutions and the high degree of individual variability within the normal population. In a preliminary report using a surface-based approach, we described several abnormalities of cortical folding in WS, including bilateral differences in position and average depth of the intraparietal sulcus (IPS) (Van Essen et al., 2004). Kippenhan et al. (2005) confirmed and extended these findings using a similar approach and reported bilateral abnormalities in the parietal cortex but unilateral abnormalities in two other regions. Here, we have applied more sensitive analyses to a slightly larger data set. Our approach (Van Essen, 2005a) involves generating accurate surface reconstruc-

Received Sept. 29, 2005; revised Feb. 28, 2006; accepted March 3, 2006.

This work was supported by the National Institutes of Health (NIH) Grant R01-MH-60974 from the National Institute of Mental Health, the National Institute for Biomedical Imaging and Bioengineering, and the National Science Foundation (D.C.V.E.); National Institute of Child Health and Human Development Grant P01 HD33113-08 (U. Bellugi; J.K. and A.R. subcontract P.I.'s); NIH Grant P01-NS06833-39 (M.E.R.); and the James S. McDonnell Foundation Collaborative Activity Award (U. Bellugi; J.K. and M.E.R. subcontract Principal Investigators). We thank J. Harwell and J. Dickson for superb software development; E. Reid for excellent data analysis; U. Bellugi for valuable discussions, catalysis of this project, and infrastructural support; B. Paul, J. Stiles, F. Rose, and R. Buckner for providing scans of control subjects; D. Mills and A. Galaburda for comments on this manuscript; S. Danker for manuscript preparation; L. Rohde for figure preparation; and C. Wu Nordhal for suggesting the *t*-statistical maps.

Correspondence should be addressed to Dr. David C. Van Essen, Department of Anatomy and Neurobiology, Washington University School of Medicine, 660 South Euclid Avenue, St. Louis, MO 63110. E-mail: vanessen@brainvis.wustl.edu.

DOI:10.1523/JNEUROSCI.4154-05.2006

 0270-6474/06/265470-14$15.00/0

tions for each individual; using maps of sulcal depth (distance from the cerebral hull) as objective measures of cortical shape; registering each individual surface to a target surface-based atlas that itself is derived from many individual subjects; and characterizing group differences using a variety of quantitative analyses.

Our results include four findings of broad interest: (1) localized folding abnormalities in WS are substantially more numerous than reported previously; (2) the pattern of abnormalities shows an unexpectedly high degree of bilateral symmetry; (3) folding abnormalities occur in a broad swath that spans all cortical lobes yet avoids major portions of the frontal, occipital, and temporal cortices; and (4) hemispheric asymmetry in the pattern of convolutions is less pronounced in WS than in control subjects. We hypothesize that WS folding abnormalities arise from alterations in the size and/or connectivity of particular subsets of cortical areas. Hence, these abnormalities may have important implications for understanding the neurobiological basis of the WS behavioral phenotypes and for elucidating the developmental mechanisms that contribute to altered neural circuitry.

Materials and Methods

Sixteen WS individuals (age, 13–52 years; mean, 24 years) and 13 normal young adults (age, 19–29 years; mean, 22 years) were scanned at the University of California, San Diego (UCSD). In addition, 24 normal young adults (age, 18–24 years) were scanned at Washington University (WU) in St. Louis. The institutional review boards of both institutions approved all procedures involving human subjects. All participants and, if appropriate, their parents or guardians provided informed written consent for the study. Classification of WS subjects was based on both clinical and genetic criteria (Korenberg et al., 2000). Additional demographic information is provided in supplemental Table 1 (available at www.jneurosci.org as supplemental material).

The MRI data consisted of sagittal T1-weighted anatomical images obtained with a 1.5 T scanner (Vision; Siemens, Erlangen, Germany) using the magnetization-prepared rapid gradient echo sequence and a standard circularly polarized head coil. The inversion time (20 ms) and delay time (200 ms) were the same at both institutions, and the flip angle was nearly the same (10° at UCSD; 9° at WU). The acquired voxel dimensions were 1 mm^3 at UCSD [repetition time (TR), 11.4 ms; echo time (TE), 4.4 ms] and $1 \times 1 \times 1.25$ mm at WU (TR, 9.7 ms; TE, 4.0 ms). The data included one (occasionally two) scans per individual at UCSD and four scans per individual at WU. In all cases, the available data were coregistered to correct for interscan head motion and resampled to 1 mm^3 voxels in 711-2B atlas space (Buckner et al., 2004). Our atlas target represents the space of Talairach and Tournoux (1988) as implemented by Lancaster et al. (1995). Given that the average brain volume is smaller in WS than controls, volume registration should result in a small differential effect on linear brain dimensions for the two groups. However, it is unlikely that the results would be substantially different if our analyses had been performed on native brain scans rather than volume-registered data (see supplemental material, available at www.jneurosci.org).

For the UCSD scans, and for some of the WU scans, structural MRI volumes were processed with gain field correction to improve segmentation quality. The 13 UCSD-scanned normals were used as the primary control group for comparisons, to avoid potential confounds related to different scanner characteristics. Parallel analyses were performed using the WU normal controls, yielding similar, although not identical, results (see supplemental Fig. 6, available at www.jneurosci.org as supplemental material). All of the groups were balanced for gender (8 of 16 were females in the WS group, 7 of 13 were females in the UCSD control group, and 12 of 24 were females in the WU control group). Four of the WS subjects were left-handed, whereas all of the control subjects were right-handed. To address whether handedness contributed to group differences, additional analyses of left–right asymmetries were performed using just the 12 confirmed right-handed WS subjects.

In brief, cortical segmentations were generated using the SureFit method [http://brainvis.wustl.edu/surefit/ (Van Essen et al., 2001)]. SureFit generates fiducial surface reconstructions that aim for midway through the cortical thickness (layer 4; see supplemental Fig. 1, available at www.jneurosci.org as supplemental material). The mid-thickness surface is preferable to the gray–white boundary or the pial surface as a substrate for surface-based registration, because it provides a relatively unbiased representation of sulcal versus gyral regions. In contrast, a gray–white surface model overrepresents sulcal regions, and a pial surface model overrepresents gyral regions.

An automated error-correction algorithm removed most of the topological and other errors in the initial SureFit segmentation. However, substantial manual editing was typically needed in some regions. Editing was most extensive in and near the hippocampal fissure, where the cortex is thin and therefore especially difficult to segment automatically. Once error-correction was completed on each segmentation, a fiducial surface was generated, and the margins of the cerebral cortex were manually identified along the medial wall (see supplemental Fig. 1*C*,*D*, available at www.jneurosci.org as supplemental material).

Sulcal depth maps (Van Essen, 2004a, 2005a) were generated for each individual hemisphere by measuring the linear distance from each node in the fiducial surface tessellation to the nearest point on a separate cerebral hull surface that wrapped around the hemisphere but did not encroach into sulci [Van Essen (2005a), compare his Fig. 1]. The sulcal depth measure is similar but not identical to the average convexity measure of Fischl et al. (1999). Subsequent processing was done using Caret software (http://brainmap.wustl.edu/caret/). Surfaces for each hemisphere were inflated, flattened, and mapped to a spherical configuration. A set of six standard landmarks was drawn on each individual hemisphere using criteria described previously [http://brainvis.wustl.edu/help/landmarks_core6/landmarks_core6.html (Van Essen, 2005a); see also supplemental Fig. 1*C*,*D*, available at www.jneurosci.org as supplemental material]. All landmarks were readily discernible in both hemispheres of all subjects, and the criteria for identifying landmark terminations were consistently applicable to each hemisphere. A single trained individual performed all segmentations and landmark assignments, thereby minimizing the risk of criterion variation across cases.

Target atlas. The target for registration was the population-average PALS-B12 atlas, which was generated by averaging the landmarks from 12 normal subjects after rigid-body alignment of the individual spherical maps (Van Essen, 2005a). We used a hybrid set of landmarks generated by averaging landmarks from both the left and right hemispheres (after mirror-flipping the 12 left-hemisphere landmarks before averaging them with the 12 right-hemisphere landmarks). This left–right hybrid target allowed comparisons between right and left hemisphere data sets registered to a common, unbiased reference frame. Separate analyses using hemisphere-specific landmark targets confirmed the main findings (see supplemental Fig. 2, available at www.jneurosci.org as supplemental material).

The landmark-constrained registration algorithm used in this study aims to minimize areal distortions in regions lying between landmarks, although significant distortions are inevitable because the surfaces are constrained to a sphere [Van Essen (2005a), his Figs. 4, 5]. The algorithm is otherwise unaffected by shape characteristics of non-landmark sulci and gyri, including features such as the IPS that vary greatly between individuals and (as shown in Results) between groups. It differs in this respect from surface-based registration algorithms that aim to maximize the correspondence of continuously varying shape attributes [http://surfer.nmr.mgh.harvard.edu/ (Fischl et al., 1999); see Discussion].

Resampling of registered surfaces. Surfaces of individual hemispheres were resampled to the standard mesh (73,730 nodes) of the PALS-B12 atlas. This allowed each hemisphere from each subject to be viewed in a variety of configurations in a single Caret application, thereby facilitating a variety of comparisons across subjects and across groups. In effect, the registration and resampling processes define what constitute corresponding locations in each individual hemisphere and the atlas. These correspondences reflect the assumptions imposed by the particular choices of landmarks and registration algorithm and thus are different from the correspondences yielded by alternative registration methods, whether volumetric or surface based (see Discussion).

Surfaced-based morphometry. Sulcal depth maps from each individual

were averaged across groups to generate average sulcal depth maps. Depth-difference maps were used to determine the magnitude of differences between groups. The *t*-statistic maps were generated by computing a *t*-statistic value (assuming unequal variance) at each node on the individual depth values in the WS and control groups. The issue of multiple comparisons is a major one, given that the *t* tests were performed on 69,378 nodes (excluding noncortical nodes along the medial wall of the atlas hemisphere). Three methods were used to take chance fluctuations into account and thereby test for statistical significance.

For the cluster-size analyses, the *t*-statistic map for each hemisphere was thresholded at a cutoff level of $t > 3$; the distortion-compensated surface area of each positive (*t* more than +3) and negative (*t* less than −3) cluster was determined. Compared with the other cutoff levels tested, this threshold level provided good sensitivity in detecting significant clusters and also good spatial resolution (by generally avoiding fusion of smaller clusters having distinctly separated centers, which occurred when using lower thresholds). Permutation analyses were used to determine the cutoff surface area for statistically significant cluster sizes. This approach capitalizes on the statistical characteristics of actual sulcal depth maps generated by our analysis methods and does not require any spatial smoothing or assumptions about normal distributions (cf. Nichols and Holmes, 2002). A set of 29 sulcal depth maps from the 16 WS and 13 control right hemispheres was randomly shuffled 2500 times, and *t*-statistic maps were computed (using subgroups of 16 vs 13 to match the actual subgroup numbers) for each of these shuffled maps. Each shuffled *t*-statistic map was thresholded to identify all positive and negative clusters having values of $t > 3$, and the surface area of each cluster was computed. To compensate for distortions in the average fiducial configuration, maps of distortion between each of the 12 PALS-B12 individual fiducial surfaces and the PALS-B12 average fiducial surface were generated and averaged. This average distortion map (see supplemental Fig. 3, available at www.jneurosci.org as supplemental material) was used to adjust the surface area of each cluster so that it represented the average extent when mapped back to a population of fiducial configurations. Histograms of cluster size were similar for positive and negative clusters, so they were combined and used to estimate the cutoff cluster sizes for statistical significance. These cutoffs were 239 mm^2 on the left and 240 mm^2 on the right for $p < 0.05$ (376 mm^2 on the left and 403 mm^2 on the right for $p < 0.01$). This cluster-size method is the surface-based equivalent of the suprathreshold cluster test described by Nichols and Holmes (2002), which provides strong control over the family-wise error rate (i.e., the probability of a single false positive cluster).

For the test–retest analyses (Buckner et al., 1995; Van Essen, 2005a), the WS and control populations were each subdivided into two arbitrary groups of near-equal size (eight in each WS group; six and seven in the two control groups). In the hypothesis-generating group, regions of interest (ROIs) were identified by thresholding the *t*-statistical map at *t* levels of +1.5 and −2.5 determining the surface area associated with each ROI on the average PALS-B12 fiducial surface. Regions for which the distortion-corrected ROI was above a criterion surface area (200 mm^2 for $t = +1.5$; 300 mm^2 for $t = -2.5$) were evaluated in the hypothesis-testing group by identifying corresponding subregions and testing each for significance using Bonferroni's correction for the number of ROIs tested. Different positive and negative thresholds were used because there was a slight overall bias toward negative *t*-statistic values. Choosing identical positive and negative thresholds would have excluded positive clusters of moderate size or yielded negative clusters of inordinately large size.

For the interhemispheric symmetry analyses, the product of the *t*-statistic values for the left and right hemispheres was computed for each node. After thresholding the resultant *t*-correlation map at a of *t*-correlation level of >6, the distortion-compensated surface area of each positive (*t*-correlation more than +6) and negative (*t*-correlation less than −6) cluster was determined. The cutoff surface area for statistically significant *t*-correlation clusters was determined by a permutation analysis that used the shuffled *t*-statistic maps from the left and right hemispheres of the 29 WS and control cases as input data. Random pairs of shuffled *t*-statistic maps were selected (one from the left and one from the right), and the product of these pairs was computed. This process was repeated 1500 times, and each of the shuffled *t*-correlation maps was analyzed for the distribution of cluster sizes. Histograms of cluster size from this permutation analysis resulted in threshold sizes of 111 mm^2 ($p < 0.05$) and 184 mm^2 ($p < 0.01$).

Using procedures detailed previously (Van Essen, 2005a), cross-correlation analyses were applied to all possible pairings of individual sulcal depth maps to quantify the degree of shape similarity between each pair. Multidimensional scaling (MDS) was performed on the resultant cross-correlation matrix, so that hemispheres similar in overall shape were in close proximity and hemispheres dissimilar in shape were widely separated in the two-dimensional MDS plot.

Stereotaxic spaces and three-dimensional surface analyses. Data reported by stereotaxic coordinates were mapped to an appropriate average fiducial surface from the PALS-B12 atlas data set. Each average fiducial surface was based on12 contributing individual fiducial surfaces that had been registered to a particular stereotaxic space (SPM99 or 711-2B) (Van Essen, 2005a).

Average fiducial surfaces were computed separately for the WS and control groups by computing the geometric average of the individual fiducial surfaces after resampling to the standard PALS mesh. The spatial detail preserved in each average fiducial surface benefited from the fact that they were generated from volumes registered to stereotaxic space.

Data access and scene visualization. The data sets illustrated in this study are accessible in the SumsDB database. The overall study directory (http://sumsdb.wustl.edu/sums/directory.do?dirid = 6414185) contains separate subdirectories for all of the individual figures, which are indicated in the figure legends. Each data set can be viewed on-line (using WebCaret) or off-line (using Caret software). Data sets for each figure are accessible separately using links provided in each figure legend. Each data set includes "scene visualization" capabilities that allow immediate regeneration of the exact screen display used to generate the individual panels in each figure.

Results

We compared shape characteristics of WS versus control groups in a variety of ways. Our primary approach used sulcal depth maps as an objective measure of cortical shape. After registering each individual to the PALS atlas, sulcal depth maps were used to generate group averages, group difference maps, and *t*-statistic maps. The *t*-statistic maps provide the main substrate for identifying significant clusters in each hemisphere and for analyzing symmetry across hemispheres, and they culminate in the folding abnormality maps shown in Figure 3. Subsequent figures illustrate complementary results based on cross-correlations between individual sulcal depth maps and analysis of group average and individual three-dimensional surfaces.

Sulcal depth maps: individual and population averages

Figure 1 illustrates some of the challenges inherent in comparing cortical shape characteristics between groups of human subjects. Each column shows representations of cortical shape for a different individual, using as examples the right hemispheres of two WS subjects (Case 1-WS, Case 2-WS, left columns) and two control subjects (Case 1-CON, Case 2-CON, right columns). Fig. 1*A–D* shows lateral views of the fiducial (three-dimensional) configurations of the four example hemispheres. The sheer complexity of cortical convolutions, coupled with the nature of the variability from one individual to the next, makes it difficult to evaluate group differences just by inspection of the fiducial surface configurations. Subjective comparisons are easier to make using inflated configurations (Fig. 1*E–H*), where the shape information evident in the partially smoothed convolutions is augmented by an explicit representation of sulcal depth. Darker shading corresponds to deeper locations in the fiducial configuration, and lighter shading corresponds to gyral crowns. Major sulci, such as the central sulcus (blue arrows), superior temporal

sulcus (green arrows), and Sylvian fissure (red arrows) can be readily identified. However, in many regions, the variability is so great that corresponding sulci and gyri are difficult to identify across different hemispheres. The bottom half of Figure 1 shows sulcal depth maps after registration to the PALS-B12 atlas. These are displayed on highly inflated atlas maps (Fig. 1*I–L*) and on a standard-configuration atlas flat map (Fig. 1*M–P*). Registration to the common spatial framework of the PALS atlas sets the stage for systematic and quantitative comparisons between groups.

Figure 2 shows several analysis stages used for comparing sulcal depth in WS versus control subjects. These are displayed on lateral (left columns) and medial (right columns) of the highly inflated PALS atlas left hemisphere (columns 1, 3) and right hemisphere (columns 2, 4). (Each view was tilted slightly to enhance visibility of several ROIs near the perimeter.) Maps of average sulcal depth, determined by averaging the depth values at each node across all individuals in a group, are shown for WS subjects in the top row (Fig. 2*A–D*) and for control subjects in the second row (Fig. 2*E–H*).

The differences between groups are much easier to visualize in the depth-difference maps (Fig. 2*I–L*), where red/orange regions are deeper, on average, in the control group and blue/green regions are deeper, on average, in the WS group. In many regions (red and blue), the average sulcal depth differs by >5 mm between the WS and control groups. In several regions, blue/green strips run parallel to adjacent red/yellow strips. This can occur either because of a displacement (translational shift) of a particular gyrus or sulcus in one group versus the other, or because of differences in average depth of sulci that are in register. Inspection of individual subjects can help resolve this issue (see below). In the lateral parietal and lateral prefrontal cortices in both hemispheres (Fig. 2*I*, *J*, black arrows), there are quasi-concentric patterns, in which a WS-deeper region is mostly surrounded by a ring in which the control cortex is deeper on average.

In both groups, depth variability (the SD of sulcal depth at each map location) varies widely across different regions [see also Van Essen (2005a), his Fig. 6]. The largest between-group depth differences tend to occur in regions showing high within-group variability. To adjust for the regional differences in within-group variability, a *t* statistic was computed at each surface node, based

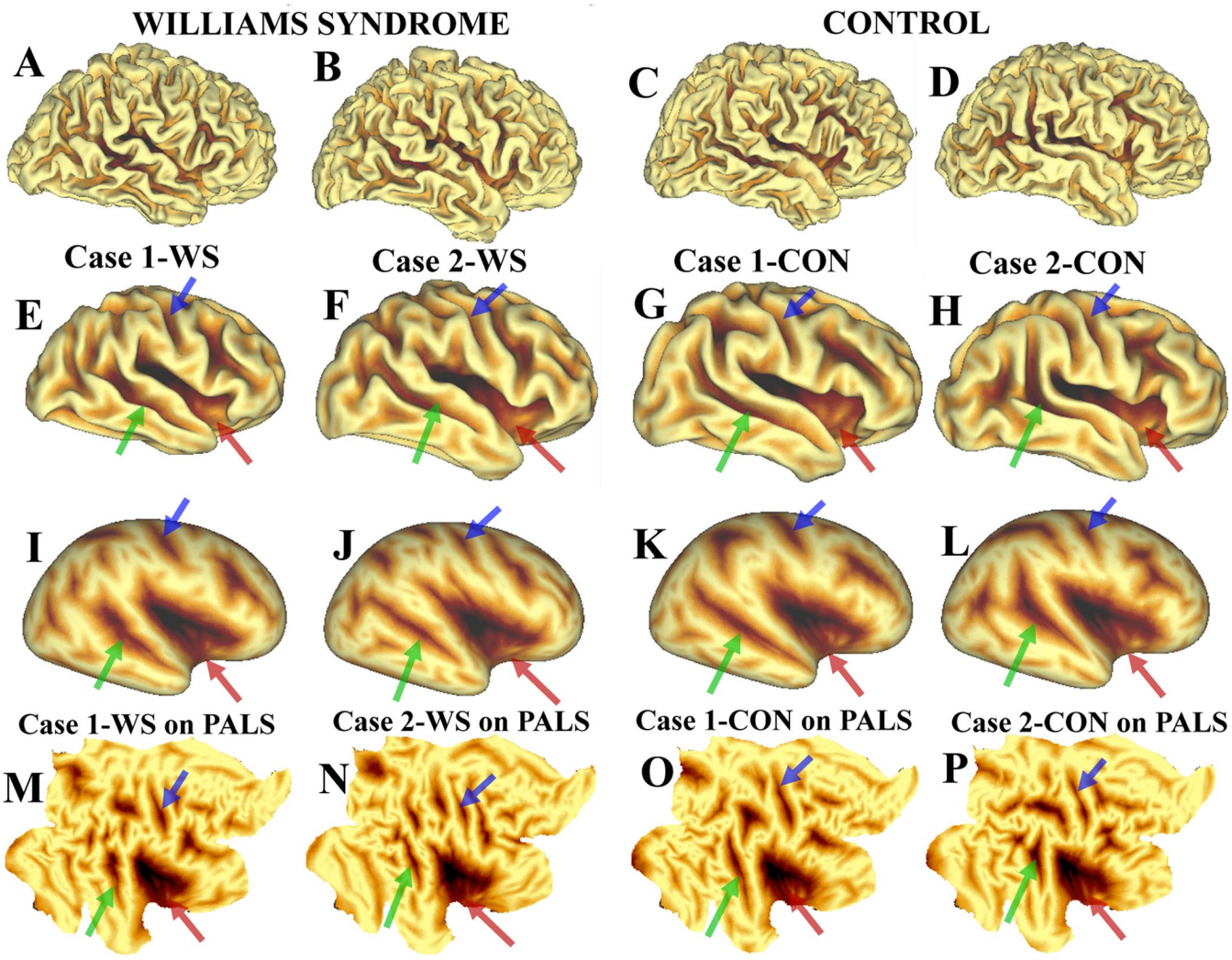

Figure 1. Individual surface reconstructions and sulcal depth maps. ***A–D***, Lateral views of fiducial surface reconstructions from the right hemispheres of two WS cases (***A***, ***B***) and two control cases (***C***, ***D***). ***E–H***, Inflated surfaces from the same four cases, with sulcal depth maps displayed on each hemisphere. ***I–L***, Sulcal depth maps on very inflated PALS atlas maps. ***M–P***, Sulcal depth maps on PALS atlas flat maps. Blue arrows, central sulcus; red arrows, Sylvian fissure; green arrows, superior temporal sulcus. The correlation coefficients (see Fig. 5*A*) for the six possible pairwise combinations of these four example sulcal depth maps ranged from 0.39 for the most dissimilar pair (Case 2-WS vs Case 1-CON) to 0.57 for the most similar pair (Case 1-WS vs Case 2-CON). Data are available at http://sumsdb.wustl.edu/sums/directory.do?dirid=6414188.

on the distribution of individual depth values at that location within the two groups. Figure 2*M–P* shows maps of *t* statistics for the 16 WS versus the 13 control subjects. The maps were thresholded at a level of $t > 2$, to display only clusters that are plausible candidates for passing statistical significance. No spatial smoothing was applied in generating these *t*-statistic maps. As in the depth-difference map, control-deeper regions are indicated in yellow and red; WS-deeper regions are indicated in green and blue. Relative to the amplitude of the depth-difference, the *t*-statistic amplitude is enhanced in regions where variability is low (e.g., the Sylvian fissure) but is reduced in regions of high variability (e.g., the IPS). As a result, the ring-like patterns noted in lateral prefrontal and lateral parietal cortices are more patchy and generally less prominent.

Comparison of the *t*-statistic maps in the two hemispheres reveals considerable symmetry in the arrangement of the larger clusters, particularly in the medial views (Fig. 2*O*,*P*). To evaluate the degree of symmetry, we took advantage of the node-by-node correspondences between left and right hemispheres established during the registration process and generated a "*t*-correlation map," in which the value at each node is the product of the corresponding left and right hemisphere *t*-statistic values for that node (Fig. 2*Q*,*R*). The *t*-correlation map was thresholded to show only regions greater than +4 (yellow/red, representing strongly correlated patterns) or less than −4 (green/blue, representing strongly anticorrelated patterns). Many of the large red/yellow *t*-correlation patches reflect correlated WS-deeper regions in each hemisphere (green arrows in the *t*-correlation maps; green/blue regions on the *t*-statistic maps); many others reflect correlated control-deeper regions in each hemisphere (red/yellow on the *t*-statistic maps). Importantly, green/blue patches in the *t*-correlation map (reflecting anticorrelated patterns in the two hemispheres) are rare, small, and collectively represent only 3% of the above-threshold regions. Anticorrelated and correlated patches would be equally common if the *t*-statistic maps in the two hemispheres were completely uncorrelated.

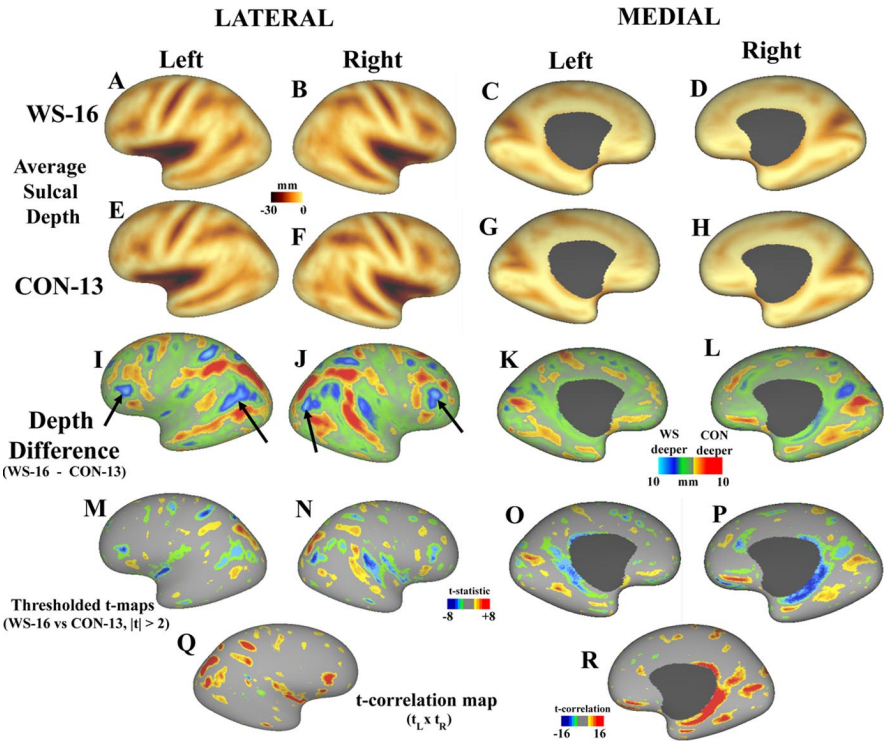

Figure 2. Initial stages of folding abnormality analysis for 16 WS cases and 13 control cases. ***A–D***, Average sulcal depth for WS subjects, displayed on the left lateral (***A***), right lateral (***B***), left medial (***C***), and right medial (***D***) PALS right hemisphere very inflated map. Darker indicates deeper on average. The lateral view is tilted dorsally, and the medial view is tilted ventrally to improve views of particular ROIs. ***E***, ***F***, Average sulcal depth for control subjects, arranged as in the top four panels. ***I–L***, Depth difference map (WS minus control). For the depth-difference maps, blue/green indicates WS deeper on average, and red/yellow indicates control deeper on average. The arrows in ***I*** and ***J*** point to WS-deeper domains encircled by a control-deeper belt. ***M–P***, *t*-statistic maps (WS-16 vs CON-13), thresholded for $t > 2$. (Note, though, that the statistical analyses summarized in Tables 1 and 2 were performed at a threshold of $t > 3$. ***Q***, *t*-correlation map, generated by taking the product of the *t*-statistic maps for the left and right hemispheres and displaying on a lateral view of the right hemisphere. The map was thresholded at a level of $t_L \times t_R > 4$, but the statistical analyses of Tables 1 and 2 are based on a threshold level of $t_L \times t_R > 6$. ***R***, Medial view of the *t*-correlation map. Data are available at http://sumsdb.wustl.edu/sums/directory.do?dirid=6414191.

Statistically significant group differences

Figure 3 shows folding abnormalities that are statistically significant by one or more of three independent methods (see Materials and Methods). In the cluster-size analysis, 14 clusters are larger than the cutoff surface area (239 mm^2 on the left, 240 mm^2 on the right) in the *t*-statistic map (Fig. 2*M–P*). In the test–retest analysis (involving eight subjects in each WS subgroup and seven or six subjects in the CON subgroups), six clusters were significant by virtue of an ROI identified in a hypothesis-generating group of subjects and confirmed in an independent hypothesis-testing group. In the symmetry analysis, 16 pairs of areas were significant by virtue of a surface area larger than 111 mm^2 in the *t*-correlation map (Fig. 2*Q*,*R*).

Altogether, 18 significant folding abnormalities in the right hemisphere and 17 significant regions in the left hemisphere were identified by one or more tests (Table 1, Fig. 3). We use the term "folding abnormality" broadly, to encompass significant differences in gyral/sulcal depth, length, orientation, and/or position. (The actual morphological basis for any given folding abnormality is best assessed by inspection of individual hemispheres, as discussed below.) Locations where the control cortex is significantly deeper than WS, on average, are indicated by red numbers plus yellow ($2 < t < 3$) and red ($t > 3$) shading; locations where the WS cortex is significantly deeper than control on average are indicated by blue numbers plus green ($2 < t < 3$) and blue ($t > 3$) shading.

Folding abnormalities in WS are distributed across a broad swath of cortex that spans all cortical lobes and encompasses approximately one-half of each hemisphere. This swath runs diagonally along the atlas flat map (Fig. 3*A*,*G*) and in the inflated hemispheres. Interestingly, many of the significant regions occur in pairs, in which a control-deeper region mainly within the sulcal cortex adjoins a WS-deeper region on or near a neighboring gyral region. This applies to five pairs of regions in both hemispheres: regions 1 and 2 (parahippocampal cortex, collateral sulcus), 3 and 4 (calcarine sulcus, anterior bank of parieto-occipital sulcus), 10 and 11 (postcentral sulcus, anterior IPS), 14 and 15 (frontal operculum of Sylvian fissure, inferior frontal gyrus), and

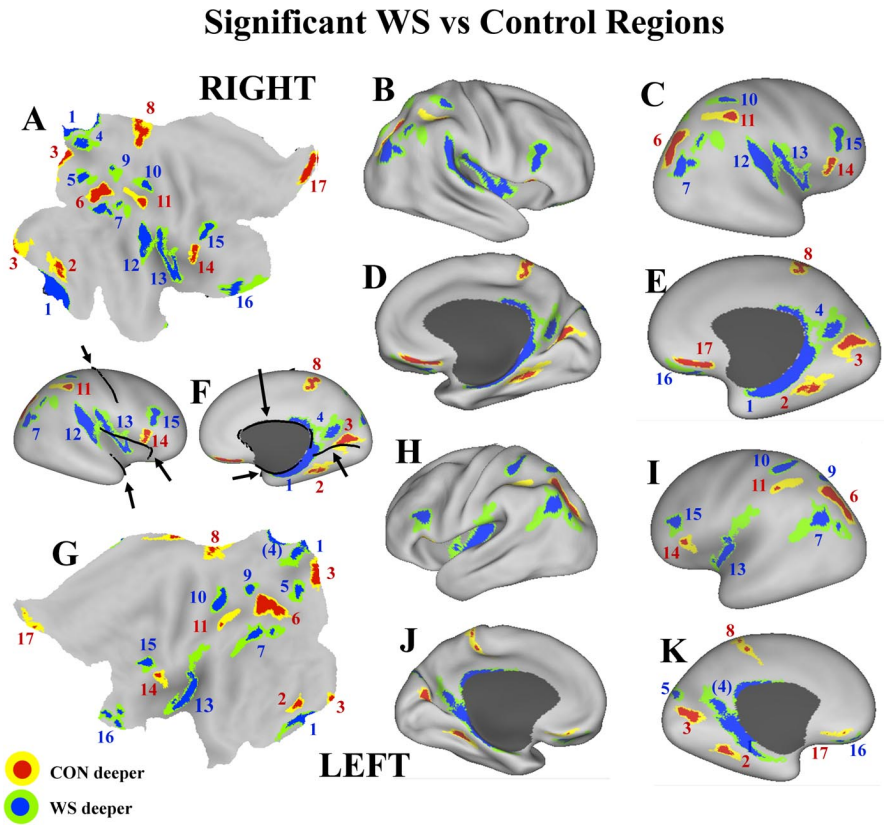

Figure 3. Maps of significant WS folding abnormalities, thresholded at $t > 2$ and displaying only regions significant by one or more tests (compare Table 1). ***A–E***, Significant regions in the right hemisphere flat map (***A***), lateral views of the inflated (***B***) and very inflated (***C***) maps, and medial views of the inflated (***D***) and very inflated (***E***) maps. Abnormally folded regions are numbered in approximate geographic sequence, from dorsoposterior to anteroventral. ***F***, Registration landmarks (black arrows, contours) overlaid on a map of WS-abnormal regions and displayed on lateral and medial very-inflated surfaces. There is no obvious systematic relationship between folding abnormalities and landmark locations. ***G–K***, Same as ***A–E***, except displayed for the left hemisphere. Red numbers and yellow/red shading, control significantly deeper than WS; blue numbers and green/blue shading, WS significantly deeper than control. In the hippocampal/parahippocampal and parieto-occipital cortices, regions 1 and 4 in the right hemisphere (Fig. 3*A–F*) jointly overlap with a single elongated region in the left hemisphere. This dual numbering (regions 1 and 4) was, nonetheless, applied to the left-hemisphere map because the parieto-occipital and hippocampal/parahippocampal regions are fundamentally different (neocortex vs archicortex/transitional cortex, respectively). Data are available at http://sumsdb.wustl.edu/sums/directory.do?dirid=6414197.

16 and 17 (olfactory sulcus, medial orbital gyrus). However, there are exceptions to this pattern. Region 8 (cingulate sulcus) is an isolated control-deeper region, and regions 12 and 13 represent isolated WS-deeper domains.

Table 1 provides additional information about the size and statistical significance of each folding abnormality. This includes the identifying number (first column), geographic location (second column), the region size (mm^2) for the left and right hemispheres (third and fourth columns, respectively), and the extent of the symmetric region (Fig. 3, t product >4) (fifth column). The third to fifth columns also indicate the statistical significance ($^*p < 0.05$, $^{**}p < 0.01$) for the permutation test (unbracketed) and the test–retest (bracketed) methods. The mean depth difference for each significant ROI (sixth and seventh columns) ranges from 1 to 6 mm.

Control analyses

Several technical issues could potentially impact the interpretation of the folding abnormalities identified in Figure 3. One issue is whether the distribution of folding abnormalities reflects a systematic bias imposed by the landmarks used to constrain surface-based registration. Figure 3*F* indicates, however, that there is no systematic relationship between the location of landmarks and folding abnormalities. In particular, some folding abnormalities (1, 3, 13) directly intersect landmarks, but the remainder are distributed at varying distances from the nearest landmark. Moreover, there is no obvious correlation between the orientation of control-deeper and WS-deeper pairs and the closest landmarks. We infer that folding abnormalities are unlikely to reflect biases introduced by the landmark-based registration process (nor by the volumetric registration process, as discussed in the supplemental material, available at www.jneurosci.org).

A second issue is whether any of the folding abnormalities reflect age rather than disease condition, given the differences in age composition of the WS and control groups (see supplemental Table 1, available at www.jneurosci.org as supplemental material). We performed two analyses to address this issue. In the first analysis, the WS cases were subdivided into an age-matched subgroup (age, 18–30 years; $n = 7$) and an age-outlier subgroup ($\geq$17 years, $n = 7$; >30 years, $n = 2$). The t-statistic maps (supplemental Fig. 4, available at www.jneurosci.org as supplemental material) showed no significant differences between the two WS subgroups in either hemisphere. A t-statistic map for the aged-matched WS subgroup compared with the entire control group showed a similar pattern as for the overall group, albeit with fewer statistically significant clusters because the sample size was smaller. The most notable difference was the absence of a WS-deeper region in the superior temporal gyrus (Fig. 3, region 12). In the second analysis, the average sulcal depth in the vicinity of a given folding abnormality was computed for each individual and was plotted as a function of age. In scatter plots of average depth versus age for the regions tested, there were no age-related trends that would confound our analysis, except for the aforementioned superior temporal gyrus region (see supplemental Fig. 5, available at www.jneurosci.org as supplemental material). We conclude that the group differences in cortical folding revealed in this study are, in general, attributable to disease condition and not age. However, additional studies will be needed to ascertain whether this conclusion applies to the superior temporal gyrus (region 12).

Given that the number of control subjects scanned under the same conditions as the WS group was relatively small ($n = 13$), it is instructive to ascertain whether a similar pattern of folding abnormalities would be revealed by analyses using a larger number of controls scanned at a different site. We compared the WS-16 group to a different group of 24 normal young adults (the "B24" group, scanned at WU; see Materials and Methods). This analysis (see supplemental Fig. 5, available at www.jneurosci.org

Table 1. Regions of significant depth difference in WS vs control subjects

		Size (mm^2), significance			Depth difference (mm)	
	Geographic location	Left	Right	Correlation	L	R
	Control deeper					
2	Collateral s.	90	114	178 *	2.7	2.4
3	Calcarine s.	269 * [*]	253 *	395 **	3.8	3.7
6	Post. intraparietal s.	551 **	528 ** [**]	639 **	5.0	6.1
8	Cingulate s.	25	191	256 **	3.0	3.8
11	Ant.intraparietal	23	125	231 **	5.4	5.6
14	Frontal operculum, SF	55	143	189 **	2.4	2.5
17	Olfactory s.	2	250 * [*]	164 *	1.1	2.9
	WS Deeper					
1	Hippocampal/parahippocampal	441 **	737 ** [**]	647 **	−2.9	−2.1
4	Parieto-occipital s.	68	192	271 **	−2.7	−4.1
5	Cuneus	165	170	279 **	−3.3	−3.7
7	Angular g.	240 *	298 * [*]	498 **	−3.0	−5.2
9	Superior parietal g.	116	25	161 *	−3.5	−3.4
10	Postcentral s.	274 *	114	250 **	−3.6	−5.2
12	Superior temporal g.		767 **			−3.7
13	Parietal operculum, insula	370**[*]	517**	726 **	−3.1	−2.6
15	Inferior frontal g.	219	267 *	390 **	−4.6	−5.4
16	Medial orbital g.	56	196	219 **	−2.0	−2.6
	Total	2921 mm^2	4888 mm^2	5493 mm^2		

Size and statistical significance of folding abnormalities identified by sulcal depth morphometry. Column 1, Focus number, in the geographic progression shown in Fig. 3. Column 2, Geographic location. Columns 3 and 4, Size and statistical significance for left (L) and right (R) hemispheres, respectively. Column 5, Size and statistical significance of the above-threshold region in the interhemispheric correlation map. *$p < 0.05$; **$p < 0.01$. Unbracketed asterisks represent cluster size method; bracketed asterisks represent test–retest method. Surface areas were computed on the PALS-B12 average fiducial surface, and then adjusted to compensate for the average distortion of the 12 contributing fiducial surfaces relative to the average fiducial surface (see Materials and Methods). Columns 6 and 7, Average depth difference for significant regions (control vs WS $t > 2$). Regions significant by the cluster size and/or test–retest methods include eight regions on the right and six on the left. Those significant only in relationship to the symmetry test include 10 regions on the left and eight on the right. That the test–retest method revealed the fewest significant regions (five on the right, two on the left) is not surprising because this is in general the most conservative of the three statistical methods used. Data are available at http://sumsdb.wustl.edu/sums/directory.do?dirid=6414224. Post., Posterior; Ant., anterior; s., sulcus; g., gyrus.

as supplemental material) revealed a similar, albeit not identical, pattern of shape abnormalities when comparing the WS-16 with the B24 group. Comparisons between the two control groups revealed only one statistically significant shape difference, in a region of the Sylvian fissure that has minimal overlap with the WS folding abnormalities. By demonstrating consistent results when comparing groups that were scanned at different sites, these findings provide a useful validation of the sulcal depth analysis approach introduced here.

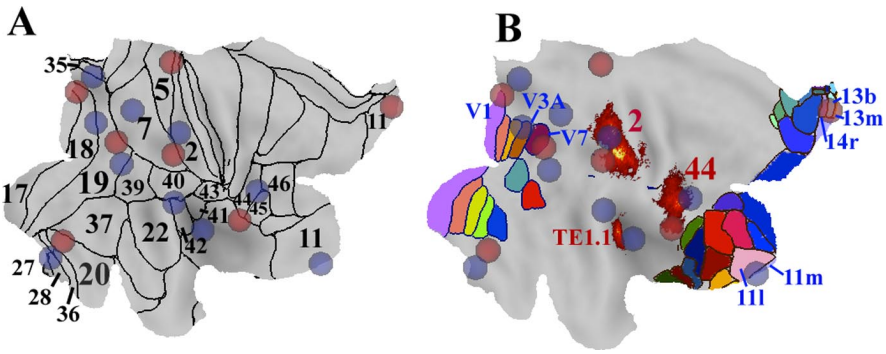

Figure 4. Comparisons of WS-abnormal regions with other experimental data. WS-abnormal regions are indicated by orange spheres for control-deeper and by blue spheres for WS-deeper regions. ***A***, Maps of Brodmann's (1909) areas in black outlines. ***B***, Visuotopic areas (Van Essen, 2004a), orbitofrontal areas (Öngur et al., 2003; Van Essen, 2005b), and probabilistic architectonic areas (2, 44, TE1.1) (Grefkes et al., 2001; Morosan et al., 2001; Amunts et al., 2004). In both maps, the average sulcal depth for the PALS-B12 right hemisphere provides the grayscale underlay. Data are available at http://sumsdb.wustl.edu/sums/directory.do?dirid=6414200.

Relationship of folding abnormalities to cortical areas

Each significant region was assigned to one or more cortical areas based on comparisons with four different cortical partitioning schemes that have been mapped to the PALS atlas (Fig. 4; Table 2, last column). As in the preceding figure, orange and blue spheres represent control-deeper and WS-deeper regions, respectively. The outlined regions (black contours) indicate the borders of cytoarchitectonic areas transposed from the original Brodmann (1909) study onto the PALS atlas flat map (with relevant Brodmann's areas labeled). In Figure 4*B*, solid colors indicate orbitofrontal architectonic areas (Öngur et al., 2003; Van Essen, 2005b) and visuotopic areas delineated in fMRI mapping studies (Van Essen, 2004a). Red/yellow graded colors indicate probabilistic maps for architectonic area 2, area 44, and the primary auditory cortex (TE1.1) (Grefkes et al., 2001; Morosan et al., 2001; Amunts et al., 2004; Van Essen, 2005a). The abnormally folded regions are distributed across many functionally distinct domains, including early sensory processing areas as well as high-level areas implicated in cognition, language, and emotion (see Discussion).

Table 2 encodes the spatial locations of folding abnormalities using both stereotaxic (three-dimensional) coordinates and surface-based coordinates (latitude and longitude) that respect the topology of the cortical sheet (Fischl et al., 1999; Van Essen, 2004a,b). Stereotaxic coordinates for the center of gravity of each folding abnormality are shown in third (left hemisphere) and fourth (right hemisphere) columns, using the average fiducial surface in 711-2B space as a reference surface. Corresponding left and right hemisphere coordinates differ by only 3–10 mm (fifth column), less than the overlap revealed by the correlation analysis (see table footnote). Surface-based coordinates (latitude and longitude) are shown in the sixth (left hemisphere) and seventh

Table 2. Spatial location of WS folding abnormalities

Focus number		Sterotaxic (x, y, z) coordinates		L–R	Latitude, longitude (θ, ϕ)		Cortical area
		Left	Right		Left	Right	Both, *left only*, **right only**
	Control deeper						
2	Collateral s.	−28, −45, −9	29, −42, −9	4	−43, −95	−43, −93	20
3	Calcarine s.	−12, −72, 6	14, −66, 9	8	−65, −166	−66, −174	17 [V1]
6	Post. intraparietal s.	−27, −72, 34	27, −71, 32	3	−8, 166	−10, 172	19, *7*; [V7]
8	Cingulate s.	−13, −48, 61	8, −46, 58	5	−19, 114	−24, 112	*1*, *2*, **5**
11	Ant. intraparietal	−45, −42, 44	39, −41, 45	6	31, 160	27, 158	7
14	Frontal operculum, SF	−46, 14, 7	41, 13, 10	5	57, −18	53, −23	44; (44, 45); ins.
17	Olfactory s.	−10, 20, −16	10, 27, −16	7	−19, −11	−16, −12	11; [11m, 13b, *14r*]
	WS deeper						
1	Hippocampal/parahippocampal	−15, −41, −6	17, −30, −7	9	−62, −72	−56, −69	27–28, 35–36, *19/26/30*
4	Parieto-occipital s.		14, −57, 15			−75, 160	**19**
5	Cuneus	−8, −83, 26	11, −87, 32	8	−46, 168	−35, 170	18; [V3A, *V3*]
7	Angular g.	−42, −72, 31	40, −76, 26	6	9, −173	0, −167	39, 19
9	Superior parietal g.	−23, −67, 52	14, −71, 51	10	−11, 147	−22, 145	7
10	Postcentral s.	−33, −44, 54	30, −40, 53	5	13, 138	20, 139	2, 5; (2)
12	Superior temporal g.		56, −33, 22			48, −142	**22/40/42**
13	Parietal operculum, insula	−37, −19, 9	39, −18, 14	8	53, −71	60, −76	40–43; (OP1, OP2, TE1.1)
15	Inferior frontal g.	−48, 15, 24	46, 18, 26	4	57, 22	57, 18	44; (44, 45)
16	Medial orbital g.	−17, 42, −14	15, 38, −15	4	0, −4	−5, −9	11; [11l, 13l, *11m*]

Columns 1 and 2, Focus number and geographic location (same as Table 1). Columns 3 and 4, Stereotaxic coordinates (711–2B space) for the geometric centers of each significant region, based on position in the average PALS-B12 fiducial surface, for the left and right hemispheres, respectively. Column 5, Separation between left (L) and right (R) hemisphere foci. Columns 6 and 7, Spherical coordinates (latitude and longitude) for the geometric center of each focus, as determined from the PALS-B12 spherical map. Column 8, Areal assignment by four different cortical partitioning schemes. Unenclosed numbers, Brodmann (1909) scheme. Numbers in square brackets, Orbitofrontal scheme of Öngur et al. (2003) or visuotopic scheme of Van Essen (2004), based mainly on Hadjikhani et al. (1998). Parentheses, Probabilistic architectonic areas from the Zilles laboratory (Grefkes et al., 2001; Morosan et al., 2001; Amunts et al., 2004; Eickhoff et al., 2006) as mapped to PALS-B12 by Van Essen (2005a). Bold and italic type indicate assignments for the left (italic) and right (bold) hemispheres, and normal type indicates assignments for both hemispheres. Data are available at http://sumsdb.wustl.edu/sums/directory.do?dirid=6414224. s., Sulcus; Post., posterior; Ant., anterior; SF, Sylvian fissure; g., gyrus; ins., insular.

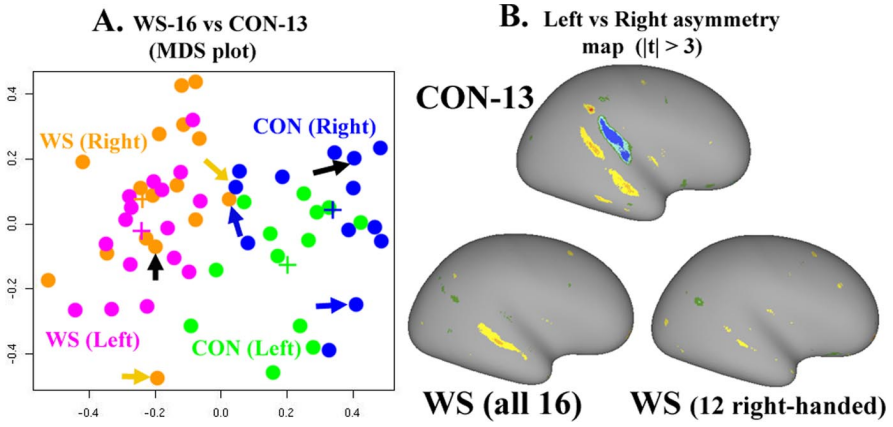

Figure 5. ***A***, MDS plot, based on cross-correlation analyses of individual sulcal depth maps, for all 58 WS and control left and right hemispheres. Each dot represents an individual hemisphere, grouped according to the color scheme indicated by the lettering in the panel. Crosses indicate the group means for the correspondingly colored group. Arrows denote exemplar cases used in the analyses shown in Figures 6 and 7, including one from each group biased toward the control side (blue arrows), one from each group biased toward the WS side (yellow arrows), and one from each group that was intermediate (black arrows). The distributions were similar for the age-matched WS subgroup (18–30 years) and the age-outlier subgroups. Likewise, the distributions for men and women were similar within the WS group and within the control group. ***B***, Map of left versus right asymmetry for control (top), all 16 WS subjects (bottom left), and the 12 right-handed WS subjects (bottom right) using *t*-statistic maps thresholded at $t > 3$. Data are available at http://sumsdb.wustl.edu/sums/directory.do?dirid=6414203.

(right hemisphere) columns in PALS-B12 space (Van Essen, 2005a).

Correlation-based analysis of sulcal depth maps

A cross-correlation and MDS analysis applied to sulcal depth maps provides a sensitive way to analyze overall similarities and differences at the level of individual subjects. This entailed computing the node-by-node cross-correlation between each pair of sulcal depth maps for the left and right hemispheres of all 29 subjects (WS and control). The resultant correlation coefficients between different hemispheres spanned a more than twofold range (0.28–0.64). Side-by-side inspection of sulcal depth maps for pairs having high correlation coefficients generally revealed strong shape similarities, whereas pairs having low correlation coefficients generally had more obvious shape differences (Fig. 1). MDS applied to the 58×58 correlation matrix yielded a two-dimensional plot in which pairs having high correlation coefficients (i.e., similar in shape) lie in close proximity and pairs having low correlation coefficients (i.e., dissimilar in shape) are widely separated. In Figure 5*A*, the 16 WS subjects are indicated by purple (left hemisphere) and orange (right hemisphere), and the 13 control subjects are indicated by green (left) and blue (right). There is virtually no overlap between the WS and control groups, and the separation between WS and control group means is highly significant for both hemispheres (randomization analysis; $p < 10^{-5}$). Interestingly, when the MDS analysis was applied to the cortex lying outside the main swath of folding abnormalities, the WS and control groups differed significantly for the right hemisphere (see supplemental material, available at www.jneurosci.org). Thus, shape abnormalities extend outside the main swath of spatially localized abnormalities, at least in the right hemisphere.

In the MDS plot, there is considerable overlap between the left and right hemisphere data points within each group. For the control group, the separation between the left and right hemisphere group means is, nonetheless, significant ($p = 0.0015$), confirming the left–right asymmetry in sulcal depth maps reported for a larger group of normal young adults (Van Essen,

2005a). For the WS group, there is no significant difference between the group means ($p = 0.76$). This signifies a greater degree of hemispheric symmetry in WS compared with control subjects. This is not attributable to the incidence of left-handed subjects (4 of 16 WS subjects, 0 of 13 control subjects) because there was no significant hemispheric asymmetry for the 12 confirmed right-handed WS subjects ($p = 0.39$).

To assess the spatial location of this group difference in hemispheric symmetry, we computed *t*-statistic maps for left versus right hemisphere sulcal depth maps. The control subjects (Fig. 5*B*, top) have prominent asymmetries in the superior temporal sulcus (right side deeper) and Sylvian fissure (planum temporale, left side deeper), consistent with that seen in a larger population of normal subjects (Van Essen et al., 2005). In contrast, WS subjects show no discernible depth asymmetry in the Sylvian fissure and a reduced depth asymmetry in the superior temporal sulcus in an analysis of all 16 subjects (Fig. 5*B*, bottom left) and of just the 12 right-handed subjects (bottom right).

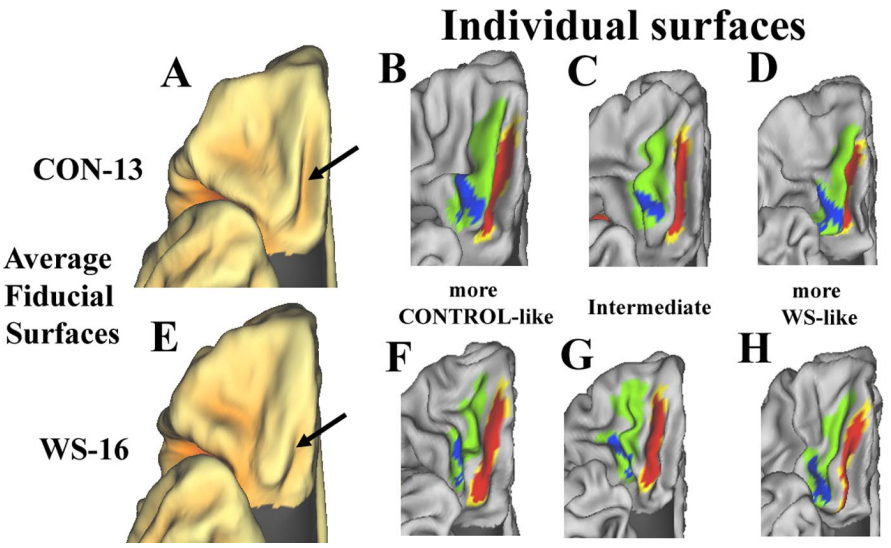

Figure 6. Folding abnormalities of the olfactory sulcus viewed on average fiducial and individual fiducial surfaces. ***A***, Ventral view of average control fiducial right orbitofrontal surface ($n = 13$), shaded by the average control sulcal depth. ***B–D***, Ventral views of individual orbitofrontal surfaces of three control subjects, ordered by their location in the MDS plot to include the most control-like hemisphere (***B***), an intermediate case (***C***), and the most WS-like case (***D***). The significant WS abnormal regions from the population analysis, mapped back to the individual surfaces, are shown using the same red/yellow and green/blue coloring as in Figure 3. ***E***, Ventral view of the average WS fiducial right hemisphere surface ($n = 16$), shaded by the average WS sulcal depth. Note the shallower and shorter olfactory sulcus (arrow) compared with the control. ***F–H***, Ventral views of individual orbitofrontal surfaces of three WS subjects, ordered by their location in the MDS plot to include a very control-like hemisphere (***F***), an intermediate case (***G***), and a very WS-like case (***H***). Note the abnormal olfactory sulcus, especially in ***F***. Data are available at http://sumsdb.wustl.edu/sums/directory.do?dirid=6414206.

Three-dimensional shape analysis in average and individual hemispheres

Direct analysis of three-dimensional shape characteristics provide useful information that is complementary to the analyses of sulcal depth described in preceding sections. This includes comparisons of the average fiducial surfaces for each group and of fiducial surfaces of individual subjects within each group.

An average fiducial surface was computed separately for the left and right hemispheres of the 16 WS and 13 control subjects. Figure 6, *A* and *E*, shows ventral views of the orbitofrontal cortex for the average right hemisphere surfaces. Each surface is shaded according to the corresponding average sulcal depth map. The olfactory sulcus (black arrows) is shallower and shorter in WS than in the control average fiducial surface.

A priori, the olfactory sulcus might be shallower in the average WS fiducial, because its position is more variable or because it is actually shallower, on average, in the individual hemispheres. To distinguish between these possibilities, we examined the fiducial surfaces of individual subjects in both groups. Figure 6, *B–D* and *F–H*, shows three representative individuals from each group that were selected objectively using their position on the MDS plot. For each group, we selected one hemisphere biased toward the control side (Fig. 6*B*,*F*), one biased toward the WS side (Fig. 6*D*,*H*), and one that was intermediate (Fig. 6*C*,*G*). (These cases are indicated in Fig. 5*A*; see legend for details.)

In each panel, folding abnormalities from the earlier group analyses are shown in the same colors as Figure 3 (red/yellow, control deeper on average; blue/green, WS deeper on average). All three control cases (Fig. 6*B–D*) have a consistently deep and long olfactory sulcus. In contrast, the olfactory sulcus is essentially absent in the leftmost WS case (Fig. 6*F*) and is notably shallow in the others (Fig. 6*G*,*H*) so that the red/yellow patch (Fig. 3, region 17) is displaced laterally onto the medial orbital gyrus. The green/blue patch (Fig. 3, region 16) includes the crown of the medial orbital gyrus in two of the control cases (Fig. 6*B*,*D*), but in all three WS cases this region is displaced laterally and lies partly in the sulcal cortex. This pattern of displacement is consistent with a selective reduction in WS subjects in the average size of cortical areas that normally occupy the olfactory sulcus (see Discussion).

In dorsoposterior views, a prominent IPS is evident in the average control fiducial surface (Fig. 7*A*) and in the three exemplar control cases (Fig. 7*B–D*). In the most WS-like control case (Fig. 7*D*), the IPS is displaced somewhat medially so that the red/yellow patch (region 6) extends onto gyral cortex. In contrast, the IPS is displaced medially and is more shallow in the average WS fiducial surface (Fig. 7*E*). The sphere centered on the IPS folding abnormality (focus 6, black arrows) is visible near the fundus of the IPS in the control surface but is centered in a gyral region and is almost entirely obscured in the WS surface. In the individual WS cases (Fig. 7*F–H*), the most control-like case (*F*) has a relatively normally positioned IPS. In the other two cases, the IPS is shallow, irregular, and displaced medially, and as a result, control-deeper region 6 is predominantly gyral.

Galaburda et al. (2001) reported that the medial termination of the central sulcus extends to the interhemispheric fissure in most control subjects but only a minority of WS subjects. In the average fiducial surfaces, there is only a slight difference in the medial extent of the central sulcus in the right hemisphere (Fig. 7*A*,*E*, red arrows) but a more prominent difference for the left hemisphere (see supplemental Fig. 6, available at www.jneurosci.org as supplemental material). In individual subjects, the central sulcus extended to the interhemispheric fissure in 11 of 13 control but only 2 of 16 WS subjects in the full data set for the right hemisphere, confirming the findings of Galaburda et al. (2001).

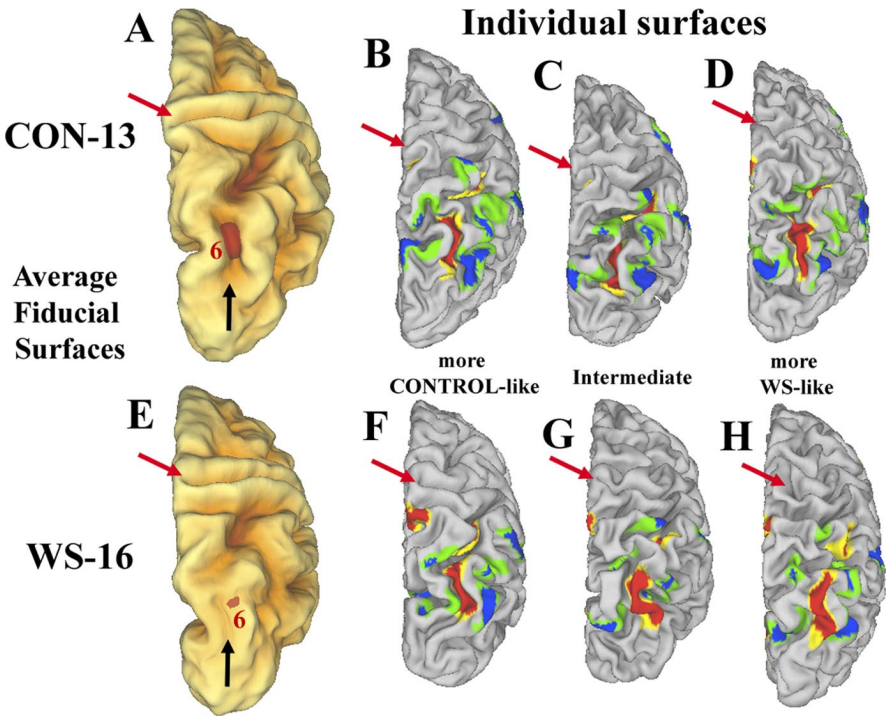

Figure 7. Folding abnormalities of the IPS viewed on average fiducial and individual fiducial surfaces. ***A***, Dorsoposterior view of average control fiducial right surface ($n = 13$), shaded by the average control sulcal depth. ***B–D***, Dorsoposterior views of individual fiducial surfaces of three control subjects, ordered as described in Figure 6. The significant WS abnormal regions from the population analysis, mapped back to the individual surfaces, are shown using the same red/yellow and green/blue coloring as in Figure 3. ***E***, Dorsoposterior view of the average WS fiducial right-hemisphere surface ($n = 16$), shaded by the average WS sulcal depth. Note the shallower and more medially positioned IPS (black arrow) compared with the control. ***F–H***, Dorsoposterior views of individual fiducial surfaces of three WS subjects, ordered as described in Figure 6. The medial tip of the central sulcus (red arrows) tends to be deeper in the control than in the WS subjects, consistent with the findings of Galaburda et al. (2001). Data are available at http://sumsdb.wustl.edu/sums/directory.do?dirid=6414209.

In general, these examples suggest that no single-shape characteristic allows categorical discrimination between WS and control group individuals. On the other hand, some characteristics show population biases that can account for the statistically significant differences seen in the population averages. Examination of individual shape characteristics in a larger set of WS and control hemispheres (left as well as right hemispheres) supported this general conclusion. Folding abnormalities in specific regions (the olfactory sulcus and IPS regions in particular) were evident in the majority of individual WS hemispheres; some but not all tended to be more pronounced in the cases that were near the extremes of the MDS plots.

Volumetric analyses

Given the highly symmetric pattern of surface-based WS abnormalities, it is of interest to know whether a volumetric analysis of group differences would reveal a comparable degree of symmetry in our data set. We analyzed volumetric group differences using an intensity-based approach [rather than attempting tissue classification as is done in the voxel-based morphometry (VBM)]. These analyses, illustrated in supplemental Figures 8 and 9 (available at www.jneurosci.org as supplemental material), yield two important conclusions. (1) The *t*-statistic maps derived from the individual volumes within each group show strong bilateral symmetry; the overall pattern is similar to that for the surface-based folding abnormalities, but with some important differences. (2) Comparison between the present intensity-based analysis and previous reports based on involving gray-matter classification (Meyer-Lindenberg et al., 2004; Reiss et al., 2004) reveals many similarities but some differences. The major difference is greater bilateral symmetry in the present study.

Discussion

This study has revealed several dozen localized folding abnormalities in WS subjects, arranged in a broad dorsoposterior to ventroanterior swath that is strikingly symmetric in the two hemispheres. Many abnormalities occur in pairs, involving a control-deeper region near the fundus of a sulcus and a nearby WS-deeper region near the crown of a gyrus. In discussing these findings, we consider four general questions: (1) How might genetically based folding abnormalities arise during development? (2) Can insights be gained by correlating folding patterns with genetic and behavioral characteristics of individual WS subjects? (3) What are the advantages, disadvantages, and complementaries of the methods used here compared with previous morphometric studies of WS? and (4) To what degree can the distinctive behavioral characteristics associated with WS be attributed to particular sets of folding abnormalities?

Developmental factors underlying folding abnormalities

One general possibility is that folding abnormalities are secondary to developmental perturbations in the size of selected cortical areas and/or the patterns of corticocortical connections. This hypothesis is motivated by a tension-based theory of cortical folding (Van Essen, 1997), which proposes that (1) mechanical tension along axons in subcortical white matter provides a primary driving force for cortical folding, and (2) the particular patterns of connectivity play a critical role in determining how the cortex folds in any given individual. By this hypothesis, abnormalities in the average size of particular cortical areas or in their connection patterns could give rise to localized folding abnormalities.

The abnormal folding of the olfactory sulcus in WS can illustrate this hypothesis. Figure 8 shows schematically how a shallower and shorter olfactory sulcus might arise in WS from a reduction in size of areas 13b and 13m, two areas that, respectively, occupy the medial and lateral banks of the olfactory sulcus (Öngur et al., 2003). During normal development, the hypothesis is that predominantly medially directed connections of area 13b and predominantly laterally directed connections of area 13m (vastly simplified in Fig. 8, *A* and *C*, relative to actual connection patterns) generate tension that results in a pair of gyral ridges separated by the olfactory sulcus. If areas 13b and 13m are physically smaller in WS, then a shallower olfactory sulcus might result from reduced mechanical tension generated by their corticocortical connections (Fig. 8*B*,*D*). A similar outcome might result from abnormal connectivity of areas 13b and 13m rather than smaller size. Although speculative, this hypothesis is neurobiologically and developmentally plausible and could readily ac-

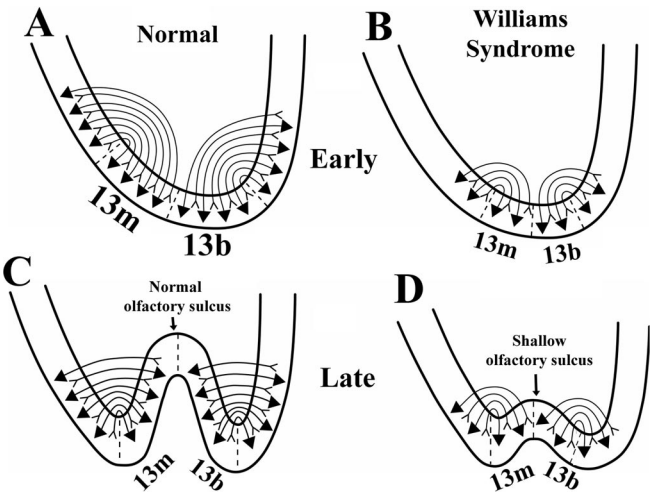

Figure 8. A schematic illustration of how reduced size of cortical areas 13b and 13m could lead to a shallower olfactory sulcus as a result of reduced mechanical tension. The schematized connection patterns are vastly oversimplified relative to known patterns of interareal connectivity in the macaque.

count for the observed symmetry of folding abnormalities. It may be possible to evaluate aspects of the hypothesis by (1) postmortem architectonic analyses of the extent of identified orbitofrontal architectonic areas and (2) *in vivo* neuroimaging methods, such as diffusion tensor imaging (Basser et al., 2000) or functional connectivity analysis (Fox et al., 2005) that provide indirect information about connectivity patterns.

By similar logic, a shallower and more medially positioned IPS might arise if cortical areas in the superior parietal lobule of WS subjects are smaller, on average, or fewer in number, consistent with reduced cortical volume (Eckert et al., 2005). Alternatively, abnormal connectivity of parietal areas might shift the IPS fundus relative to areal boundaries. In the macaque, the IPS fundus represents a transition between predominantly visual and predominantly somatosensory areas (Preuss and Goldman-Rakic, 1991; Lewis and Van Essen, 2000). In contrast, the human IPS fundus lies mainly within visual and visuomotor regions and probably has a more variable (and labile) relationship to specific areal boundaries.

The major cortical sulci appear gradually during human embryonic development, from ~16 weeks until term (Dooling et al., 1983). WS folding abnormalities occur in early-appearing sulci (calcarine and olfactory sulci and the Sylvian fissure), late-appearing sulci (inferior frontal and intraparietal sulci), and others that arise at intermediate stages and thus show no obvious correlation with this sequence.

Our finding of reduced hemispheric asymmetries in WS is consistent with evidence for greater symmetry in area 41 of WS subjects (Holinger et al., 2005) and suggests a selective effect on the developmental processes that lead to lateralization of function. This may be related to the higher incidence of left-handedness in WS subjects (26%) compared with 12% in normal individuals (Van Strein et al., 2005). However, greater symmetry in WS is not simply a consequence of handedness per se, because right-handed WS subjects are more symmetric, on average. A corollary hypothesis is that WS subjects might show greater symmetry of function in regions that are strongly lateralized in normal subjects. Along these lines, Mills et al. (2000) demonstrated greater symmetry among WS subjects in event-related potential patterns evoked during a face-matching task.

Analysis of individual differences

In MDS plots based on cross-correlation of individual sulcal depth maps (Fig. 5*A*), we found very little overlap between individual WS and control subjects. This suggests that sulcal depth morphometry has diagnostic utility by allowing most (potentially all) subjects to be identified on the basis of global shape characteristics. However, to quantify the degree of predictability using this approach, validation tests using an independent data set are needed.

The MDS approach also provides an objective framework for testing potential correlations between shape characteristics and other variables, including genetic and behavioral measures. For example, does the position of individual WS hemispheres in MDS plots correlate with specific behavioral and/or genetic characteristics (e.g., deletion breakpoints within chromosomal band 7q11.23) (Korenberg et al., 2000)? Other questions relate to the contribution of distinct genetic loci or alleles to particular folding abnormalities. For example, do WS individuals with atypically small genetic deletions (sparing of *GTF2I* and *GTF2IRD1* genes) who have relatively spared visuospatial abilities (Hirota et al., 2003) have folding abnormalities that are selectively reduced in the parietal cortex?

Methodological considerations and comparisons

Surface-based and volume-based approaches provide mostly complementary information about morphological differences between groups. VBM tests for group differences in the voxel-by-voxel distribution of gray matter, whereas surface-based morphometry as implemented here tests for group differences in the node-by-node distribution of sulcal depth. A significant group difference identified by one method may be insignificant or centered in a different location when tested by another method for a variety of reasons (compare supplemental Figs. 8, 9, available at www.jneurosci.org as supplemental material). Surface registration is superior to conventional volume-based registration in aligning identified sulci (Van Essen, 2005a) and should therefore be more sensitive to abnormalities localized to a particular gyrus or sulcus. On the other hand, VBM is more sensitive to large-scale translational or rotational displacements (e.g., petalia of the occipital and frontal lobes) (Toga and Thompson, 2003). Volumetric analysis of WS reveals a dorsal displacement of the occipital cortex, because of the relatively larger size of the cerebellum, plus a left–right asymmetry in occipital lobe gray-matter distribution (Reiss et al., 2000) that contrasts (but does not conflict) with the symmetry in the occipital cortex revealed by our surface-based analysis.

The surface-based analysis of Kippenhan et al. (2005), using a different group of WS subjects (slightly smaller, $n = 14$; better matched for age and IQ) revealed fewer folding abnormalities (4 vs 33 in the present study) and less symmetry (1 pair vs 16 pairs in the present study). The greater sensitivity of our analysis is mainly attributable to methodological factors. The registration algorithm used by Kippenhan et al. (2005) tolerates substantial local deformations to attain high correspondence between sulcal depth maps and also entailed extensive spatial smoothing before statistical analysis. The landmark-based registration used in the present study entails only modest local deformations and required no spatial smoothing.

The significant thickness differences reported by Thompson et al. (2005) between WS and control subjects were concentrated in the lateral and ventral occipito-temporal cortices, almost exclusively in the right hemisphere. This region overlaps with (but is much more extensive than) the asymmetric folding abnormal-

ity (region 12) in the present study. Cortical thickness maps and sulcal depth maps represent fundamentally different morphological measures, so there is no overt conflict between the two sets of observations. Nonetheless, the differences in spatial patterns and degree of symmetry are striking but also puzzling.

Functional correlates of morphological abnormalities

The occurrence of folding abnormalities across a broad dorsoposterior to ventroanterior swath suggests intriguing correspondences with the diverse behavioral characteristics of WS subjects. The principal cognitive features of WS (Bellugi et al., 2000; Mervis et al., 2000; Karmiloff-Smith et al., 2003; Mervis, 2003) include (1) severely impaired spatial cognition, (2) relatively spared language, (3) affinity for music, and (4) a complex emotional profile including hyperaffiliative behavior (reduced fear of strangers) despite generally increased anxiety. Folding abnormalities potentially related to each of these characteristics are considered below.

The prominent folding abnormalities in the dorsal parietal cortex (Fig. 3, regions 5–11) involve regions normally engaged in visuospatial and attentional processing (Culham and Kanwisher, 2001; Corbetta and Shulman, 2002). Impairments in visuospatial tasks (e.g., figure copying) in WS subjects may be related to reduced size or altered circuitry of these parietal lobe regions. In other vision-related regions, the folding abnormality in the calcarine sulcus (region 3) involves peripheral rather than central vision in area V1 (compare Fig. 4*B*). Given the known bias of dorsal stream areas toward the visual periphery (Baizer et al., 1991), this finding is consistent with the suggestion that WS preferentially affects the dorsal stream compared with ventral visual stream (Galaburda et al., 2001; Meyer-Lindberg et al., 2004; Atkinson et al., 2005; Eckert et al., 2005). The folding abnormality in the collateral sulcus (region 2) overlaps with the parahippocampal place area (O'Craven and Kanwisher, 2000), a part of the brain more strongly activated by viewing places compared with faces. The folding abnormality in the hippocampal region (region 1) overlaps with a region showing functional and structural abnormalities (Meyer-Lindenberg et al., 2005a).

Folding abnormalities near the planum temporale (region 13) relate to sound processing, language, and music (McDermott et al., 2003; Halpern et al., 2004). Relatively intact language with a rich vocabulary in the presence of generally impaired cognition is a hallmark of WS (Laing et al., 2005; Ypsilnati et al., 2005). WS patients characteristically exhibit heightened emotional responses to music (Levitin et al., 2004) and other sounds (Levitin et al., 2005). Given that these behavioral phenotype involves distinctive but not simply retarded functions, folding abnormalities in this region might reflect altered cortical circuitry rather than a simple size reduction of specific areas.

In the inferior frontal cortex and the frontal operculum, folding abnormalities (regions 14 and 15) involve regions implicated in language, especially in the left hemisphere (Petersen et al., 1988; McDermott et al., 2003). These abnormalities may underly the atypical features of WS language, which include developmental delay (Nazzi et al., 2005) and categorization deficits (Nazzi and Karmiloff-Smith, 2002). These regions, particularly in the right hemisphere, may also be involved in managing conflict and ambiguity, as evidenced by responses to unanticipated events (Michelon et al., 2003; Kincade et al., 2005), conflict between motor intention and sensory feedback (Fink et al., 1999), and negative feedback in the Wisconsin card-sorting test (Konishi et al., 2002). Hence, it is of interest whether WS subjects display selective deficits in such tasks, both behaviorally and in fMRI studies.

Folding abnormalities in the orbitofrontal cortex (regions 16 and 17) include subdivisions of areas 11, 13, and 14 (compare Table 1), which are part of a network involved in multisensory integration, ingestive behavior, and reward. The more medial areas adjoin and may also be components of a network mainly involved in visceral functions (Carmichael and Price, 1996; Öngur et al., 2000, 2003). In the macaque, these orbitofrontal areas are strongly connected with other parts of the limbic system, including the amygdala, that are involved in emotional behavior (Carmichael and Price, 1995). Given that the human orbitofrontal cortex is implicated in social behavior and in expressing and recognizing emotion (Bechara et al., 1997, 2000; Adolphs, 2001, 2002; Simpson et al., 2001a,b), the orbitofrontal folding abnormalities might be related to the distinctive WS emotional profile that includes hyperaffiliative behavior (Jones et al., 2000; Mervis and Klein-Tasman, 2000; Dolye et al., 2004, Reilly et al., 2004) as well as an increased prevalence of generalized anxiety and phobias (Dykens, 2003).

Previous fMRI studies comparing WS and control subjects have reported altered activations in several regions that overlap with the folding abnormalities demonstrated here, including the posterior parietal and lateral prefrontal cortices. Tasks revealing differential activations include gaze discrimination (Mobbs et al., 2004), auditory perception (Levitin et al., 2003), visuospatial construction, and attending to spatial locations (Meyer-Lindenberg et al., 2004). These initial studies may represent the tip of an iceberg in terms of the range of processing abnormalities in WS that will eventually be revealed using fMRI. The folding abnormalities identified in the present study should provide useful guides for the design and interpretation of future fMRI studies of WS.

It is of interest to compare the folding abnormalities identified in the present study with many other types of experimental data besides the various examples cited here. This is inherently challenging, given the extensive and complex literature having relevant information from neuroimaging and lesion studies in humans, plus anatomical and physiological studies of nonhuman primates. Wide-ranging data-mining explorations should be facilitated by the fact that our data sets are registered to the PALS atlas, which is associated with a rapidly growing body of experimental data that is freely available on-line in a searchable database.

References

Adolphs R (2001) The neurobiology of social cognition. Curr Opin Neurobiol 11:231–239.

Adolphs R (2002) Neural systems for recognizing emotion. Curr Opin Neurobiol 12:169–177.

Amunts K, Weiss PH, Mohlberg H, Pieperhoff P, Eickhoff S, Gurd JM, Marshall JC, Shah NJ, Fing GR, Zilles K (2004) Analysis of neural mechanisms underlying verbal fluency in cytoarchitectonically defined stereotaxic space—the roles of Brodmann areas 44 and 45. NeuroImage 22:42–56.

Atkinson J, Braddick O, Rose FE, Searcy YM, Wattam-Bell J, Bellugi U (2005) Dorsal-stream motion processing deficits persist into adulthood in Williams syndrome. Neuropsychologia 44:828–833.

Baizer JS, Ungerleider LG, Desimone R (1991) Organization of visual inputs to the inferior temporal and posterior parietal cortex in macaques. J Neurosci 11:168–190.

Basser PJ, Pajevic S, Pierpaoli C, Duda J, Aldroubi A (2000) In vivo fiber tractography using DT-MRI data. Magn Reson Med 44:625–632.

Bechara A, Damsio H, Tranel D, Damasio AR (1997) Deciding advantageously before knowing the advantageous strategy. Science 275:1293–1295.

Bechara A, Damasio H, Damasio AR (2000) Emotion, decision making and the orbitofrontal cortex. Cereb Cortex 10:295–307.

Bellugi U, Lichtenberger L, Jones W, Lai Z, St George MI (2000) The neurocognitive profile of Williams syndrome: a complex pattern of strengths and weaknesses. J Cogn Neurosci 12 [Suppl 1]:7–29.

Brodmann K (1909) Vergleichende Lokalisationslehre der Grosshirnrinde in ihren Prinzipien dargestellt auf Grund des Zellenbaues. Leipzig, Germany: J. A. Barth.

Buckner RL, Raichle ME, Petersen SE (1995) Dissociation of human prefrontal cortical areas across different speech production tasks and gender groups. J Neurophysiol 74:2163–2173.

Buckner RL, Head D, Parker J, Fotenos AF, Marcus D, Morris JC, Snyder AZ (2004) A unified approach for morphometric and functional data analysis in young, old, and demented adults using automated atlas-based head size normalization: reliability and validation against manual measurement of total intracranial volume. NeuroImage 23:724–738.

Carmichael ST, Price JL (1995) Limbic connections of the orbital and medial prefrontal cortex in macaque monkeys. J Comp Neurol 363:615–641.

Carmichael ST, Price JL (1996) Connectional networks within the orbital and medial prefrontal cortex of macaque monkeys. J Comp Neurol 371:179–207.

Corbetta M, Shulman GL (2002) Control of goal-directed and stimulus-driven attention in the brain. Nat Rev Neurosci 3:201–215.

Culham JC, Kanwisher NG (2001) Neuroimaging of cognitive functions in human parietal cortex. Curr Opin Neurobiol 11:157–163.

Dooling EC, Chi JG, Gilles FH (1983) Telencephalic develpment: changing gyral patterns. In: The developing human brain (Gilles FH, Leviton A, Dooling EC, eds), pp 94–104. Boston: John Wright PSG.

Doyle TF, Bellugi U, Korenberg JR, Graham J (2004) "Everybody in the world is my friend" hypersociability in young children with Williams syndrome. Am J Med Genet A 124:263–273.

Dykens EM (2003) Anxiety, fears, and phobias in persons with Williams syndrome. Dev Neuropsychol 23:291–316.

Eckert MA, Hu D, Eliez S, Bellugi U, Galaburda A, Korenberg J, Mills D, Reiss AL (2005) Evidence for superior parietal impairment in Williams syndrome. Neurology 64:152–153.

Eickhoff SB, Schleicher A, Zilles K, Amunts K (2006) The human parietal operculum. I. Cytoarchitectonic mapping of subdivisions. Cereb Cortex 16:268–279.

Fink GR, Marshall JC, Halligan PW, Frith CD, Driver J, Frackowiak RS, Dolan RJ (1999) The neural consequences of conflict between intention and the senses. Brain 122:497–512.

Fox MD, Snyder AZ, Vincent JL, Corbetta M, Van Essen DC, Raichle ME (2005) The human brain is intrinsically organized into dynamic, anticorrelated functional networks. Proc Natl Acad Sci USA 102:9673–9678.

Fischl B, Sereno MI, Tootell RB, Dale AM (1999) High-resolution intersubject averaging and a coordinate system for the cortical surface. Hum Brain Mapp 8:272–284.

Galaburda AM, Schmitt JE, Atlas SW, Eliez S, Bellugi U, Reiss AL (2001) Dorsal forebrain anomaly in Williams syndrome. Arch Neurol 58:1865–1869.

Grefkes C, Geyer S, Schormann T, Roland P, Zilles K (2001) Human somatosensory area 2: observer-independent cytoarchitectonic mapping, interindividual variability, and population map. NeuroImage 14:617–631.

Halpern AR, Zatorre RJ, Bouffard M, Johnson JA (2004) Behavioral and neural correlates of perceived and imagined musical timbre. Neuropsychologia 42:1281–1292.

Hirota H, Matsuoka R, Chen XN, Salandanan LS, Lincoln A, Rose FE, Sunahara M, Osawa M, Bellugi U, Korenberg JR (2003) Williams syndrome deficits in visual spatial processing linked to GTF2IRD1 and GTF2I on chromosome 7q11.23. Genet Med 5:311–321.

Holinger DP, Bellugi U, Mills DL, Korenberg JR, Reiss AL, Sherman GF, Galaburda AM (2005) Relative sparing of primary auditory cortex in Williams syndrome. Brain Res 1037:35–42.

Jones W, Bellugi U, Lai Z, Chiles M, Reilly J, Lincoln AV, Adolphs R (2000) Hypersociability in Williams syndrome: an addition to the behaioral phenotype. J Cogn Neurosci 12:30–46.

Karmiloff-Smith A, Brown JH, Grice S, Paterson S (2003) Dethroning the myth: cognitive dissociations and innate modularity in Williams syndrome. Dev Neuropsychol 23:227–242.

Kincade JM, Abrams RA, Astafiev SV, Shulman GL, Corbetta M (2005) An event-related functional magnetic resonance imaging study of voluntary and stimulus-driven orienting of attention. J Neurosci 25:4593–4604.

Kippenhan JS, Olsen RK, Mervis CB, Morris CA, Kohn P, Meyer-Lindenberg A, Berman KF (2005) Genetic contributions to human gyrification: Sulcal morphometry in Williams syndrome. J Neurosci 25:7840–7846.

Konishi S, Hayashi T, Uchida I, Kikyo H, Takahashi E, Miyashita Y (2002) Hemispheric asymmetry in human lateral prefrontal cortex during cognitive set shifting. Proc Natl Acad Sci USA 99:7803–7808.

Korenberg JR, Chen XN, Hirota H, Lai Z, Bellugi U, Burian D, Roe B, Matsuoka R (2000) VI. Genome structure and cognitive map of Williams syndrome. J Cogn Neurosci 12 [Suppl 1]:89–107.

Laing E, Grant J, Thomas M, Parmigiani C, Ewing S, Karmiloff-Smith (2005) A Love is an abstract word: the influence of lexical semantics on verbal short-term memory in Williams syndrome. Cortex 41:169–179.

Lancaster JL, Glass TG, Lankipalli BR, Downs H, Mayberg H, Fox PT (1995) A modality-independent approach to spatial normalization of tomographic images of the human brain. Hum Brain Mapp 3:209–223.

Levitin DJ, Menon V, Schmitt JE, Eliez S, White CD, Glover GH, Kadis J, Korenberg JR, Bellugi U, Reiss AL (2003) Neural correlates of auditory perception in Williams syndrome: an fMRI study. NeuroImage 18:74–82.

Levitin DJ, Cole K, Chiles M, Lai Z, Lincoln A, Bellugi U (2004) Characterizing the musical phenotype in individuals with Williams syndrome. Neuropsychol Dev Cogn C Child Neuropsychol 10:223–247.

Levitin DJ, Cole K, Lincoln A, Bellugi U (2005) Aversion, awareness, and attraction: investigating claims of hyperacusis in the Williams syndrome phenotype. J Child Psychol Psychiatry 46:514–523.

Lewis JW, Van Essen DC (2000) Mapping of architectonic subdivisions in the macaque monkey, with emphasis on parieto-occipital cortex. J Comp Neurol 428:79–111.

McDermott KB, Petersen SE, Watson JM, Ojemann JG (2003) A procedure for identifying regions preferentially activated by attention to semantic and phonological relations using functional magnetic resonance imaging. Neuropsychologia 41:293–303.

Mervis CB (2003) Williams syndrome: 15 years of psychological research. Dev Neuropsychol 23:1–12.

Mervis CB, Klein-Tasman BP (2000) Williams syndrome: cognition, personality, and adaptive behavior. Ment Retard Dev Disabil Res Rev 6:148–158.

Mervis CB, Robinson BF, Bertrand J, Morris CA, Klein-Tasman BP, Armstrong SC (2000) The Williams syndrome cognitive profile. Brain Cogn 44:604–628.

Meyer-Lindenberg A, Kohn P, Mervis CB, Kippenhan JS, Olsen RK, Morris CA, Berman KF (2004) Neural basis of genetically determined visuospatial construction deficit in Williams syndrome. Neuron 43:623–631.

Meyer-Lindenberg A, Mervis CB, Sarpal D, Koch P, Steele S, Kohn P, Marenco S, Morris CA, Das S, Kippenhan S, Mattay VS, Weinberger DR, Berman KF (2005a) Functional, structural, and metabolic abnormalities of the hippocampal formation in Williams syndrome. J Clin Invest 115:1888–1895.

Meyer-Lindenberg A, Hariri AR, Munoz KE, Mervis CB, Mattay VS, Morris CA, Berman KF (2005b) Neural correlates of genetically abnormal social cognition in Williams syndrome. Nat Neurosci 8:991–993.

Michelon P, Snyder AZ, Buckner RL, McAvoy M, Zacks JM (2003) Neural correlates of incongruous visual information. An event-related fMRI study. NeuroImage 19:1612–1626.

Mills DL, Alvarez TD, St George M, Appelbaum LG, Bellugi U, Neville H III (2000) Electrophysiological studies of face processing in Williams syndrome. J Cogn Neurosci 12 [Suppl 1]:47–64.

Mobbs D, Garrett AS, Menon V, Rose FE, Bellugi U, Reiss AlL (2004) Anomalous brain activaation during face and gaze processing in Williams syndrome. Neurology 62:2070–2076.

Morosan P, Rademacher J, Schleicher A, Amunts K, Schormann T, Zilles K (2001) Human primary auditory cortex: cytoarchitectonic subdivisions and mapping into a spatial reference system. NeuroImage 13:684–701.

Nazzi T, Gopnik A, Karmiloff-Smith A (2005) Asynchrony in the cognitive and lexical development of young children with Williams syndrome. J Child Lang 32:427–438.

Nazzi T, Karmiloff-Smith A (2002) Early categorization abilities in young children with Williams syndrome. NeuroReport 13:1259–1262.

Nichols TE, Holmes AP (2002) Nonparametric permutation tests for functional neuroimaging: a primer with examples. Hum Brain Mapp 15:1–25.

O'Craven KM, Kanwisher N (2000) Mental imagery of faces and places activates corresponding stiimulus-specific brain regions. J Cogn Neurosci 12:1013–1023.

Öngur D, Ferry AT, Price JL (2003) Architectonic subdivision of the human orbital and medial prefrontal cortex. J Comp Neurol 460:425–449.

Öngur D, Ferry AT, Price JL (2000) The organization of networks within the orbital and medial prefrontal cortex of rats, monkeys and humans. Cereb Cortex 10:206–219.

Petersen SE, van Mier H, Fiez JA, Raichle ME (1998) The effects of practice on the functional anatomy of task performance. Proc Natl Acad Sci USA 95:853–860.

Preuss TM, Goldman-Rakic PS (1991) Architectonics of the parietal and temporal association cortex in the strepsirhine primate galago compared to the anthropoid primate macaca. J Comp Neurol 310:475–506.

Reilly J, Losh M, Bellugi U, Wulfeck B (2004) Frog, where are you? Narratives in children with specific language impairment, early focal brain injury and Williams syndrome. Brain Lang 88:229–247.

Reiss AL, Eliez S, Schmitt JE, Straus E, Lai Z, Jones W, Bellugi U IV (2000) Neuroanatomy of Williams syndrome: a high-resolution MRI study. J Cogn Neurosci 12 [Suppl 1]:65–73.

Reiss AL, Eckert MA, Rose FE, Karchemskiy A, Kesler S, Chang MF, Reynolds MF, Kwon H, Galaburda A (2004) An experiment of nature: brain anatomy parallels cognition and behavior in Williams syndrome. J Neurosci 24:5009–5015.

Schmitt JE, Watts K, Eliez S, Bellugi U, Galaburda AM, Reiss AL (2002) Increased gyrification in Williams syndrome: evidence using 3-D MRI methods. Dev Med Child Neurol 44:292–295.

Simpson JRJ, Drevets WC, Gusnard DA, Raichle ME (2001a) Emotion-induced changes in human medial prefrotonal cortex: I. During cognitive task performance. Proc Natl Acad Sci USA 98:683–687.

Simpson JRJ, Drevets WC, Snyder AZ, Gusnard DA, Raichle ME (2001b) Emotion-induced changes in human medial prefrotonal cortex: II. During anticipatory anxiety. Proc Natl Acad Sci USA 98:688–691.

Talairach J, Tournoux P (1988) Coplanar stereotaxic atlas of the human brain. New York: Thieme Medical.

Thompson PM, Lee AD, Dutton RA, Geaga JA, Hayashi KM, Eckert MA, Bellugi U, Galaburda AM, Korenberg JR, Mills DL, Toga AW, Reiss AL (2005) Abnormal cortical complexity and thickness profiles mapped in Williams syndrome. J Neurosci 25:4146–4158.

Toga AW, Thompson PM (2003) Mapping brain asymmetry. Nat Rev Neurosci 4:37–48.

Van Essen DC (1997) A tension-based theory of morphogenesis and compact wiring in the central nervous system. Nature 385:313–318.

Van Essen DC (2004a) Surface-based approaches to spatial localization and registration in primate cerebral cortex. NeuroImage [Suppl] 23:s97–s107.

Van Essen DC (2004b) Organization of visual areas in macaque and human cerebral cortex. In: The visual neurosciences (Chalupa L, Werner JS, eds), pp 507–521. Cambridge, MA: MIT.

Van Essen DC (2005a) A population-average, landmark- and surface-based (PALS) atlas of human cerebral cortex. NeuroImage 28:635–662.

Van Essen DC (2005b) Surface-based comparisons of macaque and cortical organization. In: From monkey to brain: proceedings of a Fyssen Foundation Colloquium, June 2003 (Dehaene S, ed), pp 3–20. Cambridge, MA: MIT.

Van Essen DC, Snyder AZ, Raichle ME, Rose FE, Bellugi U (2004) Differences in cortical shape in Williams syndrome subjects compared to normal humans revealed by surface-based analysis. Soc Neurosci Abstr 30: 239.12.

Van Essen DC, Dickson J, Harwell J, Hanlon D, Anderson CH, Drury HA (2001) An integrated software system for surface-based analyses of cerebral cortex. JAMA 8:443–459.

Van Essen DC, Harwell J, Hanlon D, Dickson J (2005) Surface-based atlases and a database of cortical structure and function. In: Databasing the brain, from data to knowledge: neuroinformatics (Koslow SH, Subramaniam S, eds), pp 369–388. Hoboken, NJ: Wiley.

Van Strien JW, Lagers-Van Hasen GC, Van Hagen JM, De Coo IFM, Frens MA, Van Der Gees JN (2005) Increased prevalences of left-handedness and left-eye sighting dominance in individuals with Williams-Beuren syndrome. J Clin Exp Neuropsychol 27:967–976.

Ypsilanti A, Grouios G, Alevriadou A, Tsapkini K (2005) Expressive and receptive vocabulary in children with Williams and Down syndromes. J Intellect Disabil Res 49:353–364.